Neurobiology of Disease 209 (2025) 106906

Contents lists available at ScienceDirect

Neurobiology of Disease

journal homepage: www.elsevier.com/locate/ynbdi

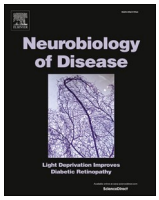

Pharmacodynamic biomarkers responsive to mutant huntingtin lowering in a Huntington's disease mouse model

Deanna M. Marchionini [a,*], Stef De Lombaerde [b], Joëlle van Rijswijk [c,d], Franziska Zajicek [b,d], Liesbeth Everix [b,d], Alan Miranda [b,d], Mari J. Aaltonen [e], Carleen M. Kluger [e], Thomas Wild [e], Aglaia Kakoulidou [e], Jannis Gundelach [e], Tim Fieblinger [e], Joachim Fentz [e], Jim Rosinski [a], John Obenauer [f], Jonathan R. Greene [f], Longbin Liu [a], Ignacio Munoz-Sanjuan [a], Marleen Verhoye [c,d], Jeroen Verhaeghe [c,d], Jonathan Bard [a], Steven Staelens [c,d,1], Daniele Bertoglio [b,c,d,1]

[a] CHDI Management, Inc., The Company That Manages the Scientific Activities of CHDI Foundation, Inc., 350 7th Ave, Suite 200, New York, NY, 10001, USA
[b] Molecular Imaging Center Antwerp (MICA), University of Antwerp, Campus Drie Eiken, Room D.UC.059, Universiteitsplein 1, B-2610 Wilrijk, Belgium
[c] Bio-Imaging Lab, University of Antwerp, Campus Drie Eiken, Building UC, Room 111, Universiteitsplein 1, B-2610 Wilrijk, Belgium
[d] μNeuro Centre of Excellence, University of Antwerp, Campus Drie Eiken, Building N, D.N. 110, Universiteitsplein 1, B-2610 Wilrijk, Belgium
[e] Evotec International GmbH, Anna-Sigmund-Str. 5, 82061, Neuried, Germany
[f] Rancho Biosciences, 16955 Via Del Campo, Suite 200, San Diego, CA, 92127, USA

1. Introduction

Huntington's disease (HD) is a progressive autosomal dominant neurodegenerative disorder caused by the expansion of a CAG repeat within the huntingtin (*HTT*) gene that encodes an expanded polyglutamine (polyQ) tract in the HTT protein. Lowering of mutant huntingtin (mHTT) protein in cerebrospinal fluid (CSF) from people with HD (PwHD) treated with *HTT*-lowering reagents has been observed in several clinical trials (Tominersen, Roche/Ionis: ClinicalTrials.gov, NCT05686551 (McColgan et al., 2023); WVE-003, Wave Life Sciences, NCT05032196; Branaplam, Novartis, NCT05111249; PTC518, PTC Therapeutics, NCT05358717 (Gao, 2024)). However, there remains a critical need for early, quantitative and spatial biomarkers of efficacy to track the biological benefits of *HTT*-lowering agents, including those currently in development and approaching clinical trials.

Currently, most clinical *HTT*-lowering-directed therapeutic strategies are achieving 35–50 % reduction in *HTT* (Spronck et al., 2019; Spronck et al., 2021; Tabrizi et al., 2019; Tabrizi et al., 2020), with exceptions that UniQure's AMT-130, delivered with AAV5, has not reported on mHTT lowering levels (Farag et al., 2024) and Skyhawk's SKY-0515 reported 72 % *HTT* mRNA lowering in blood (https://www.skyhawktx.com/news, July 2024). We wanted to detect CNS-wide changes in mHTT within the common range being pursued clinically using the LacQ140 HD mouse model (Marchionini et al., 2022), which allows for m*Htt* lowering of both *Htt1a* (Sathasivam et al., 2013) and full-length *Htt* transcripts in a regulatable fashion to approximately 40–50 % throughout the body in a Q140 KI context (Menalled et al., 2003). The LacQ140 model exhibits homogenous lowering of m*Htt* across all cells due to the ubiquitous β-actin (Patrinostro et al., 2018) promoter that we used to drive LacIR expression; this homogenous m*Htt* lowering is likely more similar to what may be achieved by small molecule *HTT* lowering strategies.

We previously reported that early m*Htt* lowering (at 2 months of age) greatly delayed the accumulation of mHTT protein inclusion bodies (IBs), ameliorated behavioral and transcriptional dysregulation, and delayed the increase of neurofilament light chain (NfL) levels in CSF. However, all these benefits were attenuated by 12 months of age. Late m*Htt* lowering (at 8 months of age) did not improve transcriptional dysregulation, and behavioral benefits were diminished at 12 months of age, suggesting that earlier m*Htt* lowering was more beneficial (Marchionini et al., 2022). Transcriptional dysregulation is correlated to the presence of diffuse or aggregated nuclear mHTT, and cytoplasmic IBs track with behavioral phenotypes in the R6/2 mouse model (Landles et al., 2020). Here, we sought to understand proteome integrity using the LacQ140 model and identify biological pathways and proteins that exhibited long-term responsiveness to m*Htt* lowering using a multimodal approach.

To facilitate the interpretation of regional pharmacological effects of

* Corresponding author at: CHDI, 350 7th Ave, Suite 200, New York, NY 10001, USA.
E-mail address: Deanna.Marchionini@CHDIFoundation.org (D.M. Marchionini).
[1] Contributed equally.

https://doi.org/10.1016/j.nbd.2025.106906
Received 24 January 2025; Received in revised form 20 March 2025; Accepted 6 April 2025
Available online 9 April 2025
0969-9961/© 2025 The Authors. Published by Elsevier Inc. This is an open access article under the CC BY license (http://creativecommons.org/licenses/by/4.0/).

candidate therapeutics targeting mHTT, we recently validated non-invasive imaging agents specific for aggregated mHTT and responsive markers, such as phosphodiesterase 10a (PDE10A), to give insight into the timing, durability, magnitude and spatial therapeutic effects of specific m*Htt*-lowering approaches (Bertoglio et al., 2018; Bertoglio et al., 2022a). Consequently, we sought to investigate the *in vivo* changes in imaging biomarkers in relation to early or late lowering of m*Htt* in the LacQ140 mouse model. Specifically, we explored the ability of PET imaging tracers, [^{11}C]CHDI-180R (mHTT aggregates) and [^{18}F]MNI-659 (PDE10A), to identify time- and region-specific pharmacological effects to inform on their applicability in interventional paradigms (Bertoglio et al., 2022a; Herrmann et al., 2021). Using autoradiography, we further examined whether imaging agents for striatal markers with diminished expression in PwHD (specifically PDE10A, and striatal dopamine receptors) (Antonini et al., 1998; Beaumont et al., 2016; Fazio et al., 2020; Liu et al., 2020; Russell et al., 2016; Weeks et al., 1996) can detect the protective effects of m*Htt* lowering interventions in mice in a time-dependent manner and serve as pharmacodynamic response indicators for m*Htt* lowering with translational potential.

2. Methods

2.1. Animals

All animal experiments were performed according to guidelines by the National Institutes of Health (Bethesda, MD, USA) for the care and use of laboratory animals as well as in accordance with the EU legislation (EU directive 2010/63/EU) and reported according to the ARRIVE guidelines. Humane endpoints were used. The study protocol was approved by the Ethical Committee for Animal Testing (ECD #2018–82) at the University of Antwerp (Belgium). Male and female heterozygous (HET) LacQ140 mice (Marchionini et al., 2022) with a mean ± standard deviation CAG size of 165 ± 8 and wild-type (WT) littermates were group housed (uniform sex, genotype, treatment) or single housed (for imaging studies) with environmental cage enrichment (play tunnels, plastic bones, Enviro-dri, and Bed-o'cobs) and fed *ad libitum*. To maintain normal m*Htt* expression levels during embryonic development, the lactose analog isopropyl β-D-1-thiogalactopyranoside (IPTG) was added to chow (2.5 mg/g) or water (10 mM) to derepress the *LacQ140* allele and administered to pregnant dams beginning at E5, with the resultant offspring maintained on this schedule post-weaning. In cohorts where m*Htt* was repressed, IPTG was withdrawn at either 2 or 6 months of age. As a control for IPTG effects, WT mice received IPTG for the duration of the experiment; an additional 2 groups of WT mice did not receive IPTG and were sacrificed at 6 and 12 months of age. All experimenters were blinded until completion of analyses. Mice were either euthanized by live decapitation or perfused with 4 % paraformaldehyde for tissue fixation after anesthesia with isoflurane (5 % for induction). Before perfusion, the loss of toe pinch reflex was assessed to ensure that the correct level of anesthesia was achieved. Groups of mice were used for PET imaging, autoradiography (ARG) and MSD (n = 24–27/group), Proteomics and qPCR (n = 10/group) and immunohistochemistry (IHC; n = 6–8).

2.2. Radioligand synthesis

2.2.1. [^{11}C]CHDI-180R – mHTT aggregate detection

The radioligand was prepared using an automated synthesis module (Carbonsynthon I, Comecer, The Netherlands) as previously described (Bertoglio et al., 2022a). [^{11}C]CHDI-180R was prepared *via* single-step carbon-11 labeling starting with 0.5 mg of precursor in 0.5 ml of dimethylformamide, which was reacted with [^{11}C]MeI, in the presence of Cs_2CO_3 (2.5–3 mg) for 3.5 min at room temperature. The radiochemical purity was greater than 99 % as determined using a Kinetex EVO C18, 5 μm, 150 × 4.6 mm (Phenomenex) HPLC column, with acetonitrile/0.05 M sodium acetate pH 5.5 (30/70 *V*/V) as mobile phase, at a flow of 1.5 ml/min, with UV absorbance set at 280 nm.

2.2.2. [^{18}F]MNI-659 – PDE10A detection

Radioligand was prepared by adapting our previously described procedure (Bertoglio et al., 2018) to the automated AllinOne synthesis module (Trasis) using a cassette system built *in-house* (Bertoglio et al., 2022a). Synthesis of [^{18}F]MNI-659 was accomplished by reacting dried [^{18}F]fluoride with the MNI-659 tosylate precursor (7 mg) in dimethyl sulfoxide (DMSO) (1 ml) for 10 min at 90 °C. Final radiochemical purity was >99 %, as determined using a Waters Xbridge C18 5 μm 4.6 mm × 150 mm column (Waters) with acetonitrile/0.05 M sodium acetate pH 5.5 (55/45 V/V) as mobile phase, at a flow of 1 ml/min, with UV absorbance set at 230 nm.

2.3. PET imaging

2.3.1. Image acquisition

Dynamic microPET/Computed tomography (CT) images were acquired using two virtually identical Siemens Inveon PET/CT scanners (Siemens Preclinical Solution) as previously described (Bertoglio et al., 2018; Bertoglio et al., 2022a; Bertoglio et al., 2022b). Animals were anesthetized using isoflurane (induction 5 %, maintenance 1.5 %) in medical oxygen and catheterized in the tail vein for intravenous (i.v.) bolus injection of the tracer. Animals were placed on the scanner bed with the full body in the PET scanner's field of view (FOV) to allow the extraction of the image-derived input function (IDIF) from the left ventricle as previously described (Bertoglio et al., 2022b). Information regarding molar activity injected radioactivity, injected mass, body weight, and age on scan day for each radioligand at different time points and studies are reported in Supplementary Tables 1–2. Radioligands were injected with activity as high as possible to obtain good image quality and to keep the cold mass as low as possible in order not to violate tracer conditions. In all experimental paradigms, we were below the critical limit and set our target at 1.5 μg/kg for [^{11}C]CHDI-180R and 1.25 μg/kg for [^{18}F]MNI-659. PET data were acquired in list mode format. Dynamic scans lasted 60 min for both [^{11}C]CHDI-180R and [^{18}F]MNI-659. PET scans were followed by a 10 min 80 kV/500 μA CT scan on the same gantry for attenuation correction and co-registration purposes. Acquired PET data were reconstructed into 33 frames of increasing length (12x10s, 3x20s, 3x30s, 3x60s, 3x150s, and 9x300s) using a list-mode iterative reconstruction with proprietary spatially variant resolution modeling in 8 iterations and 16 subsets of the 3D ordered subset expectation maximization (OSEM 3D) algorithm (Miranda et al., 2020). Normalization, dead time, and CT-based attenuation corrections were applied. PET image frames were reconstructed on a 128x128x159 grid with 0.776 × 0.776 × 0.796 mm^3 voxels. Mice that displayed extravasation or movement artifacts during acquisition were excluded from analysis.

2.3.2. Image processing

Image analysis was performed with PMOD 3.6 software (Pmod Technologies) applying an MR-based pipeline adapting the previously described procedure. (Bertoglio et al., 2018; Bertoglio et al., 2022a) The spatial transformations were applied to the dynamic PET images and assessed for accuracy following spatial transformation. Voxels of interest (VOIs) were manually adapted from the Waxholm atlas (Johnson et al., 2010) to match each genotype and age-specific generated MR template (Supplementary methods). Time-activity curve (TAC) for the striatum, motor cortex, hippocampus, thalamus, and cerebellum were extracted for quantification.

2.3.3. Kinetic modeling

Absolute quantification for [^{11}C]CHDI-180R was performed to calculate the total volume of distribution based on image-derived input function ($V_{T\ (IDIF)}$) as a non-invasive surrogate of the V_T. Kinetic modeling fitted regional TACs using the Logan model (Logan et al.,

1990) and the IDIF with the start of the linear regression (t^*) calculated according to the maximum error criterion of 10 % as previously described (Bertoglio et al., 2022b). Since only negligible metabolism of [^{11}C]CHDI-180R was observed in different genotypes and ages (parent compound >95 %), no correction for radiometabolites was applied. Parametric $V_{T\ (IDIF)}$ maps were generated through voxel-based graphical analysis (Logan) (Logan et al., 1990) using the IDIF as input function, and were then cropped using the brain mask of the MRI template, represented as group averages, and overlaid onto a 3D mouse brain template for anatomical reference.

For the quantification of [^{18}F]MNI-659 the non-displaceable binding potential (BP_{ND}) was determined by fitting the regional TACs using the simplified reference tissue modeling (SRTM) (Gunn et al., 1997). The striatum was selected as the receptor-rich region and the cerebellum was the receptor-free region (reference region) (Bertoglio et al., 2018; Bertoglio et al., 2021). Parametric BP_{ND} maps were generated using SRTM2 (Wu and Carson, 2002) with the k_2' as calculated with SRTM (Gunn et al., 1997). The individual images were smoothed with an isotropic gaussian filter (0.5 mm in full width at half maximum), cropped using the brain mask of the MRI template, represented as group averages, and overlaid onto each condition- and age-specific 3D brain template for anatomical reference. The estimated mHTT lowering effect was calculated as the difference between LacQ140 mice subjected to m*Htt* lowering (either as of 2 or 6 months) and LacQ140 mice without lowering and normalized to the total phenotypic difference, estimated as the delta between LacQ140 and WT mice. Thus, the mHTT lowering response of each molecular target was estimated as follows:

$$\text{mHTT lowering response } (\%) = \frac{\text{LacQ140}_{(2M\ 0r\ 6M)} - \text{LacQ140}}{\text{LacQ140} - \text{WT}} * 100$$

2.4. Immunostaining

After perfusion, brains were removed and cryopreserved in 30 % sucrose, embedded in OCT and stored at −80 °C. Immunohistochemistry was performed as previously described (Zeitler et al., 2019). Primary antibodies included the following: monoclonal mouse anti-mHtt PHP2 (1:3000, HD Community Biorepository at the Coriell Institute for Medical Research (Ko et al., 2018)), and polyclonal chicken anti-NeuN (1:1000, MilliporeSigma, ABN91P). An antigen retrieval step was carried out for 30 min at 80 °C in citrate buffer (0.01 M Na-citrate buffer, pH 6.0). Secondary antibodies included the following: anti–mouse IgG (1:1000, HRP-conjugated, Abcam, ab205719) and anti–chicken IgY (H + L) (1:1000, *CF*-647, Sigma-Aldrich, SAB4600179). PHP2 signal was amplified using Biotinyl-Tyramide (TSA kit, Akoya, SAT700001EA, 1:100 in 0.003 % H_2O_2/0.1 M Borate Buffer, pH 8.5) and with streptavidin conjugated with DyLight Alexa-Fluor 488 (1:500 in 0.1 % Triton/Tris buffered solution; Thermo Fisher Scientific, S32354). Sections were mounted using aqueous mounting medium (AntiFade Fluorescence Mounting Medium, Abcam, ab104135) in 12-well glass-bottom plates (CellVis, P12–1.5H-N) suitable for imaging with the Opera Phenix High Content Screening system (PerkinElmer Inc.).

Automated image acquisition was conducted using the Opera Phenix High Content Screening system and Harmony software v.4.9 (PerkinElmer Inc.) using a × 40/1.1 numerical aperture water immersion objective (resulting xy-resolution of 0.29 × 0.29 μm per pixel) for imaging of mHTT inclusions. Image analysis scripts for characterization and quantification of mHTT inclusions were developed in Acapella Studio v.5.1 (PerkinElmer Inc.). Individual cells within tissue sections were identified using the DAPI signal and a general nuclei detection script based on the Acapella "nuclei detection B" algorithm. Specifically, the algorithm was defined to exclude objects with an area smaller than 200 pixels. Neurons were identified based on NeuN signal intensity. Cells with a nuclear NeuN-intensity of at least 2× background were defined as neurons. The analysis of mHTT inclusions was performed based on the PHP2 signal intensity. First, a texture image was calculated using the SER Spot Texture Filter of Acapella v.5.1 at a scale of 3 pixels. Spots were initially segmented as objects with a texture signal above 0.2. Objects smaller than 5 pixels (0.42 μm^2) or with an intensity lower than 2 times that of the mean intensity of the unfiltered image were excluded from the analysis. The mean spot intensity had to be 2-fold higher compared with the local surrounding (4 px wide ring around each spot). PHP2 spots per NeuN+ neuron in the striatum were quantified. The striatum was manually outlined in labelme software (version 4.5.5) on adjacent sagittal sections starting at 1.725 mm lateral to the midline. The resulting outline was then imported into Acapella for region specific analysis. Image data from 3 sections were averaged per animal, and 6–8 animals per treatment group were used for statistical evaluation. Nuclear and extranuclear spots were identified based on localization or exclusion respectively to the DAPI nuclear stain. Spot sizes were measured as single spot-data and for further analysis of the distribution the data was summarized in bins of 0.5 μm^2.

2.5. Proteomics

Striata were weighed and homogenized in 10 μl/mg Syn-PER Reagent (#87793 ThermoScientific, 1× Roche Protease Inhibitor) with micropestles on ice. Debris was cleared by centrifugation (1200 x*g*, 10 min, 4 °C) and the homogenate was collected from the supernatant. Homogenate was lysed in SDC buffer (1 % Sodium deoxycholate, 10 mM Tris (2-carboxyethyl) phosphine hydrochloride, 40 mM 2-Chloroacetamide, 75 mM Tris pH 8.5). Protein concentration was determined by BCA assay. 80 μg from each sample was proteolytically digested by Trypsin/LysC. Peptides were desalted using Strata-X-C cartridges (Phenomenex) and lyophilized. Samples were analyzed by liquid-chromatography tandem mass-spectrometry (LC-MS/MS) on a Thermo Orbitrap Exploris mass spectrometer equipped with an Easy nLC-1000 UPLC system (Thermo Fischer Scientific). Samples were loaded with an auto sampler onto a 40 cm fused silica emitter (New Objective) packed in-house with reversed phase material (Reprusil-Pur C18-AQ, 1.9 μm, Dr. Maisch GmbH) at a maximum pressure of 950 bar. The bound peptides were eluted over a 125 min gradient and sprayed directly into the mass spectrometer using a nanoelectrospray ion source (ProxeonBiosystems). The mass spectrometer was operated in data-independent acquisition mode (DIA) for single-shot analysis.

Raw files were processed with the DIA-NN software suite (Demichev et al., 2020) version 1.7.12 for peptide and protein identification and quantification using a curated Uniprot database (Swissprot and varsplic including proteins isoforms, version 2020_03). The false discovery rate (FDR) for protein identification was set to 1 %. All peptides were required to have a minimum peptide length of 8 amino acids and a maximum of two missed cleavages. The inference of protein groups from Dia-NN output was performed using a custom algorithm based on Nesvizhskii and Aebersold (Nesvizhskii and Aebersold, 2005).

The intensities were normalized and converted to protein group $\log_2$ intensities including protein groups with minimum two detected precursors. Principal component analysis (PCA) plots were used to identify and remove outlier samples. Proteins were filtered out if they were identified by fewer than 3 peptides or had measured values in fewer than 2/3 of the replicates. Differential expression tests were performed using the R packages Limma and Bioconductor (Biobase) and required a fold change of 1.2 between groups and an FDR adjusted *p*-value of 0.1. Outlier samples were detected using PCA plots and heatmaps and were removed from the analyses.

Proteins identified to be significantly dysregulated in LacQ140, compared to WT, at 6, 9 and 12 months of age defined the LacQ140 disease signature. To examine the extent that m*Htt* lowering could prevent the LacQ140 disease signature, a phenotype reversal analysis was performed using the Posterior probabilities method (Marchionini et al., 2022). The following categories and boundaries for reversal classification were applied:

super.reversal (S) = -Infinity to −1.3.

full.reversal (F) = −1.3 to −0.7.
partial.reversal (P) = −0.7 to −0.2.
negligible.reversal (N) = −0.2 to 0.2.
exacerbation (E) = 0.2 to Infinity.

Proteins that were dysregulated at 6, 9 and 12 months of age were further used for enrichment analysis. A union list of 710 unique proteins dysregulated at 6, 9, and 12 months was derived as the "HD union" protein list. This list of proteins was tested for gene set over-representation against the GOBP gene set collection using the enricher function within the R clusterProfiler package (Ashburner et al., 2000; Yu et al., 2012). Gene sets with a clusterProfiler q < 0.05 were deemed significant. The HD union proteins within each gene set were then scored for normalization based on their overall reversal probabilities as determined above using the posterior probability method. In this way, the percentage of HD union proteins present in each gene set was determined.

2.6. Autoradiography

Brains were dissected and snap frozen in 2-methylbutane and stored at −80 °C. *In vitro* autoradiography studies were performed on the same animals as the *in vivo* PET studies (upon sacrifice), using [^{3}H]CHDI-180, [^{3}H]T-773, [^{3}H]SCH23390, and [^{3}H]Raclopride as previously reported (Bertoglio et al., 2022a). *Ten μm-thick sections were prepared on a cryostat and slides were* equilibrated by immersion into assay buffer (50 mM Tris-HCl pH 7.4; 120 mM NaCl; 5 mM KCl; 2 mM $CaCl_2$; 1 mM $MgCl_2$) for 20 min at room temperature. [^{3}H]T-773 (MA = 79 Ci/mmol), [^{3}H]SCH23390 (MA = 81 Ci/mmol), and [^{3}H]Raclopride (MA = 76 Ci/mmol) were prepared by Novandi Chemistry AB, whereas [^{3}H]CHDI-180 was prepared by Pharmaron (MA = 84 Ci/mmol). Slides and commercial tritium activity standards (American Radiolabeled Chemicals, ART 0123C, and ART 0123B) were exposed on Tritium Phosphor Screen (GE Healthcare, Fuji BAS-TR 2025 E) for 24 h ([^{3}H]T-773), 90 h ([^{3}H]SCH23390 and [^{3}H]Raclopride), or 120 h ([^{3}H]CHDI-180). Stored radiation energy on the screen was scanned using a Phosphorimager (GE Healthcare, Typhoon FLA 7000). Densitometric data analysis of radioligand binding was performed using ImageJ (National Institute of Health, USA). Quantification was performed by converting the mean grey values into binding density (fmol/mg) calculated from standard curves using commercial microscale tritium standards (American Radiolabeled Chemicals).

2.7. Statistical analysis

Statistical analysis was performed in GraphPad Prism v9.1 (GraphPad Software). Data are expressed as the mean ± standard deviation (s.d.) or standard error of the mean (SEM). To choose the appropriate statistical test, data were checked for normality using the Shapiro-Wilk test. If the normality test was not passed, non-parametric statistical tests were used. Imaging, histological, and autoradiography data were analyzed using a one-way ANOVA with Tukey's multiple comparison test. Correlation coefficients were calculated with Pearson's correlation analysis. Statistical significance was set at $p < 0.05$, with the following standard abbreviations used to reference P values: ns, not significant; *$p < 0.05$; **$p < 0.01$; ***$p < 0.001$; ****$p < 0.0001$. Detailed statistical information for each experiment is provided in the corresponding figure legends. Summary of sex and n for histology and proteomics can be found in Supplementary Table 3.

3. Results

3.1. ~50 % mHtt lowering delayed the accumulation of mHTT aggregation

The LacQ140 mouse model was generated by crossing the LacQ140 to $Tg^{ACTB\text{-}lacI^*Scrb}$ (Cronin et al., 2001; Marchionini et al., 2022). The default state of the LacQ140 mouse is whole-body repression of m*Htt* due to Lac repressor binding to the Lac operators. Administration of IPTG disrupts binding between the Lac repressor and operators, resulting in a derepressed state and maximal expression of m*Htt* (Fig. 1A). As reported previously (Marchionini et al., 2022), m*Htt* mRNA and protein expression levels were approximately 50 % lowered in the absence of IPTG (Supplementary Fig. 1). IPTG administration was started at E5 and maintained for the duration of the experiment or removed at 2 or 6 months-of-age to induce early or late m*Htt* lowering (Fig. 1B).

We longitudinally tracked the accumulation of mHTT *in vivo* using [^{11}C]CHDI-180R microPET imaging in LacQ140 and WT mice from 3 to 12 months of age (Fig. 2 and Supplementary Table 4). We observed a temporal accumulation in [^{11}C]CHDI-180R PET $V_{T(IDIF)}$ in the striatum of the LacQ140 compared to WT which was statistically significant as early as 3 months of age ($p < 0.001$; Fig. 2B,C). Both early and late m*Htt* lowering significantly reduced the mHTT aggregated species detected by PET [^{11}C]CHDI-180R imaging (Fig. 2B-C). In line with the immunostaining (Fig. 3), the early m*Htt* lowering animals displayed a statistically significant reduction in mHTT aggregates when compared to the late lowering group at 12 months of age in the striatum ($p < 0.0001$; Fig. 2B-C) as well as other investigated brain structures (Supplementary Fig. 2). At 12 months of age, we estimated 75.0 % and 52.8 % striatal mHTT aggregate lowering *via* microPET in early and late m*Htt* lowering groups, respectively. Moreover, autoradiography with radiolabeled [^{3}H]CHDI-180 from striatal samples from the same mice at 12 months of age was in agreement with the *in vivo* microPET imaging, with early and late

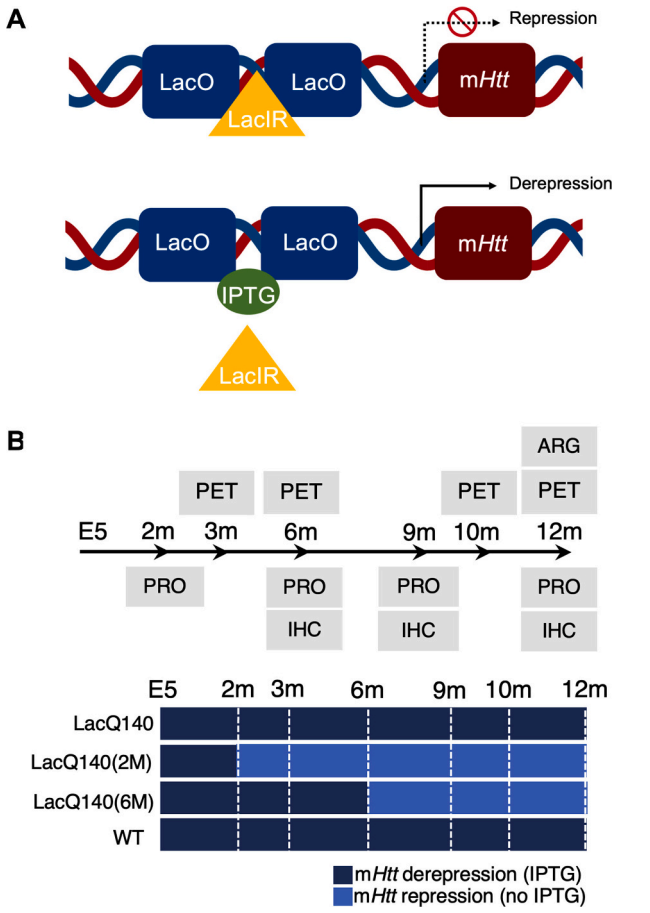

Fig. 1. Schematic overview of LacQ140 allele and overview of experimental timelines. (A) Schematic of the $Tg^{ACTB\text{-}lacI^*Scrb}$ transgene and the $Htt^{LacQ140}$ allele. The default state of the $Htt^{LacQ140/+}$; $Tg^{ACTB\text{-}lacI^*Scrb/+}$ mouse is global repression of m*Htt* due to Lac repressor binding to the Lac operators. (B) Overview of timeline of experimental paradigm. Proteomics (PRO), positron emission tomography (PET), autoradiography (ARG).

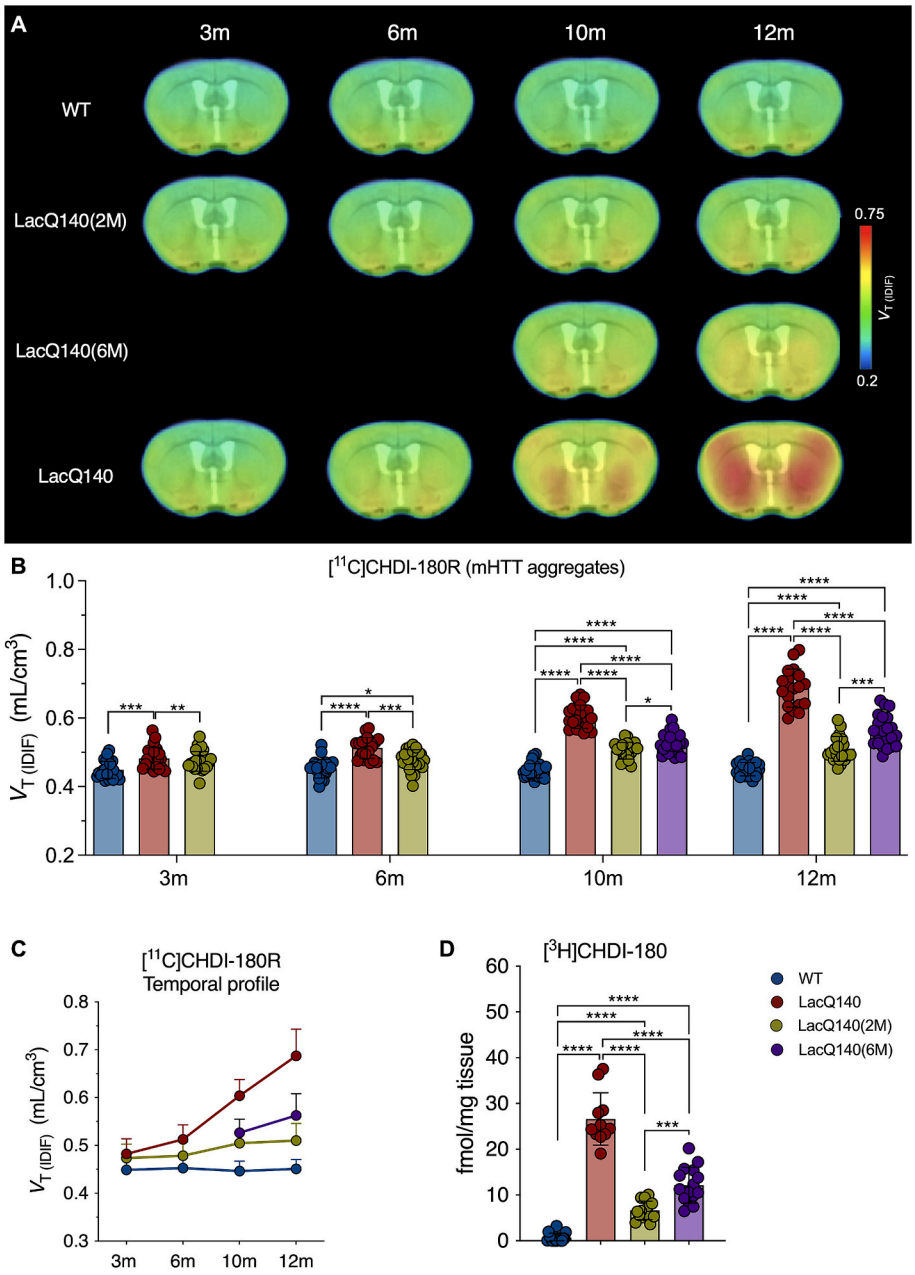

Fig. 2. *In vivo* imaging of reduced mHTT aggregates over time. (A) Mean [^{11}C]CHDI-180R $V_{T\ (IDIF)}$ parametric PET images in the coronal plane of WT, LacQ140(2M), LacQ140(6M) and LacQ140 at 3, 6, 10, and 12 months of age. (B) ■WT, ■ LacQ140, ■ LacQ140(2M), ■ LacQ140(6M). Quantification of striatal [^{11}C]CHDI-180R $V_{T\ (IDIF)}$. One-way ANOVA at each time point. 3 m: $F(2,34) = 6.8$, $p = 0.0032$, 6 m: $F(2,64) = 23.2$, $p < 0.0001$, 10 m: $F(3,88) = 135.1$, $p < 0.0001$, and 12 m: $F(3,81) = 125.4$, $p < 0.0001$; $n = 20$–27 mice/ group. (C) Temporal profile of the striatal [^{11}C]CHDI-180R $V_{T\ (IDIF)}$. (D) Specific autoradiographic binding of [^{3}H]CHDI-180 in the striatum at 12 months of age. One-way ANOVA, $F(3,53) = 137.3$, $p < 0.0001$ ($n = 11$–17 mice/group). *$p < 0.05$, ***$p < 0.001$, ****$p < 0.0001$. Data are shown as mean ± SD.

m*Htt* lowering resulting in 73.8 % and 51.4 % striatal mHTT aggregate reduction, respectively (Fig. 2D).

To obtain a better understanding of the mHTT species present following m*Htt* lowering, we characterized the mHTT aggregation profile at different ages with immunohistochemistry. Diffuse and IB nuclear PHP2 immunostaining was observed in the striatum of LacQ140 by 6 months of age; by 9 months of age there was additional emergence of extranuclear IBs; and by 12 months of age, there was robust accumulation of nuclear and extranuclear IBs, as well as a loss of diffuse nuclear immunoreactivity (Fig. 3A-C). Early m*Htt* lowering significantly delayed the accumulation of nuclear and extranuclear IBs at all ages examined; the impact on extranuclear IBs was profound (Fig. 3E-G, I-J). Mice with late m*Htt* lowering did not exhibit a significant reduction in nuclear IBs; however, extranuclear IB formation was delayed (Fig. 3H, I-J). In the striatum of the LacQ140, nuclear IBs increased in size with age, while extranuclear IBs, once formed, minimally increased in size. Early m*Htt* lowering delayed growth of IBs in the nucleus but had negligible impact on extranuclear IBs towards a larger size. Late m*Htt* lowering had limited impact on nuclear or extranuclear IB size (Fig. 3K-L).

3.2. Early mHtt lowering delays synaptic proteomic dysfunctions

A signature of dysregulated striatal proteins was identified by proteomic analysis in the LacQ140. First, we compared striatum from WT, with and without IPTG at 6 and 12 months of age, to determine if consumption of IPTG resulted in proteomic changes. We did not identify

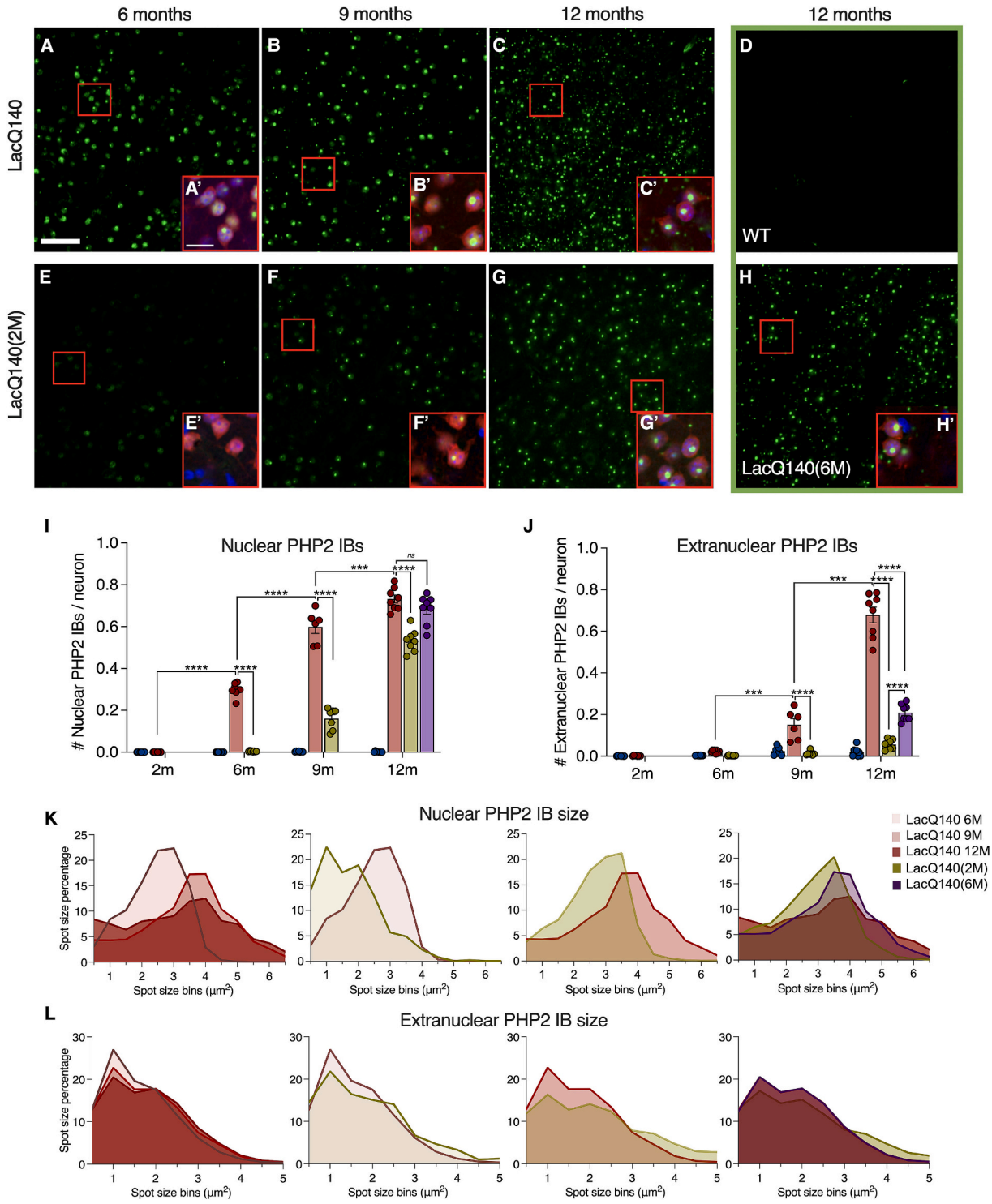

Fig. 3. m*Htt* lowering leads to long-term striatal reduction in mHTT protein. (A-C) Representative PHP2 immunolabeling of the LacQ140 striatum at 6, 9 and 12 months of age; (D) PHP2 in the striatum of 12 months old WT; (*E*-G) PHP2 in the early m*Htt* lowering [LacQ140(2M)] striatum at 6, 9 and 12 months of age. (H) PHP2 in the late m*Htt* lowering [LacQ140(6M)] striatum at 12 months of age. Scale bar: 50 μm. (A'-H′) insets with NeuN (red), PHP2 (green), and DAPI (blue) co-labeling; Scale bar: 25 μm. The arrow points to a nuclear IB and the arrowhead highlights an extranuclear IB. (I) Nuclear and (J) extranuclear quantitation of PHP2 spot density per neuron at 2, 6, 9 and 12 months of age. ■ WT, ■ LacQ140, ■ LacQ140(2M), ■ LacQ140(6M). One-way ANOVA $F(7,53) = 293.7$, $p < 0.0001$ (nuclear) and $F(7,53) = 185.6$, $p < 0.0001$ (extranuclear), followed by Tukey's multiple comparisons. ***$p < 0.001$, ****$p < 0.0001$, ($n = 6$–8 mice/ group); data are shown as mean ± SEM. WT group was not included in statistical analysis. (K) Nuclear distribution of PHP2 spots per bin size in the striatum of LacQ140 at 6, 9 and 12 months of age. (L) Extranuclear distribution of PHP2 spots per bin size in the striatum of LacQ140 at 6, 9 and 12 months of age. (For interpretation of the references to colour in this figure legend, the reader is referred to the web version of this article.)

any proteins that were significantly different (Supplementary Table 5). Next, we compared proteins that were differentially expressed in the LacQ140 *versus* WT + IPTG striatum at 2, 6, 9 and 12 months of age (Supplementary Table 5). The only proteins that were different at 2 months of age were HTT and Huntingtin associated protein 40 (HAP40/F8a1). At 6, 9 and 12 months of age there were 238, 426, and 489 differentially expressed proteins, respectively, in the LacQ140 striatum compared to WT (FDR adjusted $p < 0.1$ and a fold change of at least 1.2-fold in either direction; Supplementary Table 5). All dysregulated proteins were analyzed for gene sets over-representation analysis (GSORA) pathway enrichment, revealing nodes of dysregulation of proteins collectively involved in cellular ion homeostasis, G-protein coupled receptor signaling pathways, and proteins involved in synaptic plasticity and the consolidation of learning and memory processes in the striatum of the LacQ140 mouse model (Fig. 4A).

To determine the probability that m*Htt* lowering attenuated LacQ140 proteomic dysregulation on a protein-by-protein basis, we employed the posterior probability-based method (Marchionini et al., 2022) to assign a reversal probability for each protein under the m*Htt* lowering scenarios. Early m*Htt* lowering persistently partially preserved the proteome over time, with the number of dysregulated LacQ140 striatal proteins strongly attenuated (by 42 % at 6 months; 47 % at 9 months and 50 % at 12 months). In contrast, late m*Htt* lowering had negligible impact on the proteomic disease signature, showing an 8 % and 4 % attenuation in the number of dysregulated striatal proteins at 9 and 12 months of age, respectively (Fig. 4B, Supplementary Table 6). We

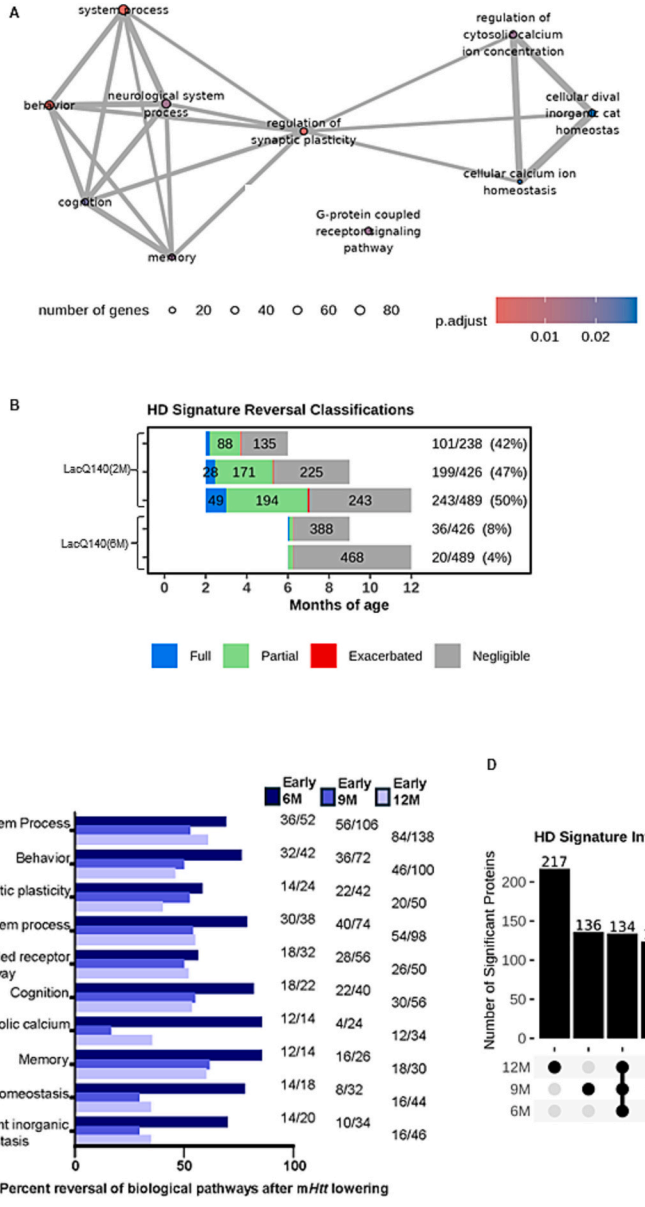

Fig. 4. Proteomic dysregulation is delayed with early but not late m*Htt* lowering. (A) Dysregulated proteins in LacQ140, compared to WT, were identified at 6, 9 and 12 months of age (n = 9–10/group). Pathway enrichment revealed the top dysregulated pathways in the striatum of the LacQ140. (B) Using posterior probabilities, we identified the percentage of dysregulated proteins that were reversed with early or late m*Htt* lowering at 6, 9 or 12 months of age. Early m*Htt* lowering fully or partially reversed proteomic dysregulation in 101, 199 and 243 proteins at 6, 9 and 12 months of age. Reversal is presented as a percentage and as the number of reversed proteins divided by the total number of LacQ140 striatal dysregulated proteins at each age. (C) The top dysregulated pathways in the LacQ140 were examined for reversal at each timepoint. The number of proteins identified in the GSORA pathway are indicated, along with the number of proteins fully or partially reversed. (D) Overlap in dysregulated proteins at each age is presented. We identified a total of 714 dysregulated proteins in the striatum of the LacQ140 at 6, 9 and 12 months of age. 134 proteins were dysregulated at all ages.

further examined the probability of reversal after m*Htt* lowering across our top dysregulated pathways found in the striatum of the LacQ140. Early m*Htt* lowering led to robust preservation of proteins across all the top dysregulated biological pathways, with diminished benefits over time. Late m*Htt* did not reverse any of our most dysregulated pathways (0 %, not shown; Fig. 4C).

We further identified a 134-protein LacQ140 signature of striatal proteins that were persistently dysregulated at 6, 9, and 12 months of age (Fig. 4D, Supplementary Table 7). We identified 26 proteins that were responsive to m*Htt* lowering at all three ages (Table 1, Supplementary Table 7). Examination of specific examples of commonly dysregulated proteins in HD showed that early m*Htt* lowering had a significant probability of preserving proteins including PDE10A, dopamine receptor D1 (DRD1), phosphodiesterase 1B (PDE1B), and angiotensin-converting enzyme (ACE) for, at least, up to 12 months of age (Fig. 5).

3.3. PDE10A is a responsive biomarker to mHtt lowering

Exploiting the outcome of the proteomics analysis, we selected PDE10A as a candidate protein to track the temporal effect of m*Htt* lowering in LacQ140 mice. PDE10A levels were unchanged in the striatum of LacQ140 at 2 months of age, as measured by proteomics (Fig. 5), suggesting our early m*Htt* lowering timepoint occurred prior to PDE10A dysregulation. Based on the proteomic analysis, early m*Htt* lowering partially maintained PDE10A protein levels in the striatum out to 12 months of age, while late m*Htt* lowering did not improve PDE10A levels (Fig. 5). PDE10A microPET imaging with [^{18}F]MNI-659 revealed that PDE10A was significantly reduced in the striatum of the LacQ140 as early as 3 months of age (Fig. 6A-C and Supplementary Table 5). Early m*Htt* lowering resulted in a significant preservation of PDE10A levels at 3 and 6 months of age but was diminished by 10 months of age. Additionally, late m*Htt* lowering was unable to rescue PDE10A levels measured at 10 and 12 months of age (Fig. 6A-C). Specific binding of [^{3}H]T-773 autoradiography demonstrated that early m*Htt* lowering partially maintained PDE10A signal in the striatum out to 12 months of age (Fig. 6D).

3.4. The dopamine system is partially responsive to mHtt lowering

Another component of HD pathogenesis is the loss of dopaminergic D1 and D2 receptors, involved in direct and indirect dopamine pathways, respectively (Reiner and Deng, 2018). D1 dopamine receptors were significantly reduced in the striatum of the LacQ140 by 6 months of age, compared to WT, as measured by proteomics (Fig. 5). Early m*Htt* lowering partially preserved DRD1 protein expression at 6, 9 and 12 months of age (Fig. 5). We were unable to detect sufficient peptides for dopamine D2 receptor (DRD2) protein, therefore no conclusions on DRD2 expression or preservation could be made with proteomics. Thus, we further performed autoradiography using [^{3}H]SCH23390 (D_1 receptors) and [^{3}H]Raclopride ($D_{2/3}$ receptors) in the striatum of 12 months old LacQ140 mice; this confirmed both D_1 and $D_{2/3}$ receptors were reduced in the striatum of LacQ140 mice, compared to WT littermates. Following early m*Htt* lowering D_1, but not $D_{2/3}$, receptors were partially preserved. On the contrary, late m*Htt* lowering was unable to reverse the D_1 nor $D_{2/3}$ receptor loss (Fig. 7).

Table 1
Proteins that are persistently preserved with early m*Htt* lowering. Within our 134-protein LacQ140 signature, we identified 26 proteins that were partially preserved after early m*Htt* lowering at all ages examined. N = 9–10/group (mixed males, females).

Ace	Camk4	Drd1	Ngef	Ppp1r1b	Rgs9	Sipa1l3
Adcy5	Camkk2	Ephx1	Pde10a	Ppp2r2a	Rps6ka4	Tesc
Arpp19	Coch	Impdh1	Pde1b	Rap1gap	Scn4b	
Arpp21	Cyld	Inf2	Ppp1r1a	Rasd2	Sfn	

4. Discussion

There is a need for translational biomarkers that are responsive to *HTT*-lowering therapeutics, many of which have either entered clinical trials or will do so imminently. Here, we have demonstrated that aggregated mHTT protein levels were robustly responsive to m*Htt* lowering. Using an unbiased global proteomic approach, we further identified proteins that were persistently dysregulated in the LacQ140 mouse model. By analysis of the 'reversable dysregulated proteome' we identified a core set of 26 dysregulated striatal proteins across all ages evaluated, whose expression levels were persistently improved with early m*Htt* lowering. Of these, PDE10A and D_1R are immediately amenable to PET approaches (Antonini et al., 1998; Fazio et al., 2020; Turjanski et al., 1995; Weeks et al., 1996), and we propose these as long-term candidate responsive biomarkers for *HTT*-lowering strategies.

Our previous work indicates that the [^{11}C]CHDI-180R PET ligand binds to extranuclear aggregated mHTT (Bertoglio et al., 2022a; Liu et al., 2020), which is in agreement with observations in the current study, suggesting those proteoforms of mHTT are very amenable to m*Htt* lowering strategies. mHTT oligomers/fibrils/IBs, as detected by PHP2 IHC, [^{3}H]CHDI-180 ARG and [^{11}C]CHDI-180R microPET imaging, were responsive to m*Htt* lowering. Early m*Htt* lowering resulted in a delay in accumulation of nuclear and extranuclear mHTT IB number and size. While late m*Htt* lowering had no effect on the number of PHP2+ nuclear IBs, it resulted in a robust reduction in the number of extranuclear IBs. It is possible that progression of extranuclear IB formation is a late phenotype in the LacQ140 model, and our late m*Htt* lowering at 6 months of age is still early enough to delay the formation. Studies in postmortem HD brains show that there are more mHTT inclusions in the cytoplasm and dystrophic neurites than in the nucleus (DiFiglia et al., 1997; Gutekunst et al., 1999; Hickman et al., 2022; Maat-Schieman et al., 1999), suggesting this could be a relevant mHTT species to target. Furthermore, studies using HD mouse models suggest that extranuclear IBs correlate with behavioral deficits (Landles et al., 2020).

Proteomic and gene ontology biological pathway enrichment analysis on the striatum of the LacQ140 model at 6, 9 and 12 months of age revealed dysregulation in pathways associated with cellular calcium and ion homeostasis, G-protein signaling, and synaptic plasticity. In our analysis, we focused on reversal of this dysregulation after m*Htt* lowering and observed that early m*Htt* lowering resulted in robust prevention of these dysregulated pathways at 6 months of age. While there was a trend for the effects to diminish by 9 months of age, most of the pathways were still partially preserved over time. Transcriptomic and proteomic changes are not always congruent (de Sousa Abreu et al., 2009) and our proteomic findings in this study contrasts with what we previously observed in this model with transcriptional profiling, where the benefits attenuated more dramatically over time (54 % at 6 months of age to 27 % at 12 months of age *versus* 42 % and 50 % at 6 and 12 months of age, respectively, in this proteomics study) (Marchionini et al., 2022). Consistent with that same transcriptional study, we found no reversal of our top dysregulated biological pathways with late m*Htt* lowering. These findings suggest that the probability of clinical benefit of a given intervention with *HTT*-lowering therapeutics is higher when applied at early HD stages (McColgan et al., 2023).

We identified a list of 26 proteins that were dysregulated in the striatum of the LacQ140 model at 6, 9 and 12 months of age, and were preserved at all ages with early m*Htt* lowering. Most of these 26 proteins were also preserved out to 12 months of age with early m*Htt* lowering in our transcriptomics study (Marchionini et al., 2022). PDE10A and DRD1 represent biomarkers we further investigated using different imaging approaches since these are readily amenable to non-invasive PET imaging (Antonini et al., 1998; Fazio et al., 2020; Turjanski et al., 1995; Weeks et al., 1996). ACE has been previously reported to be down-regulated in a CAG-length-dependent manner (Aaronson et al., 2021) and a PET imaging ligand was recently reported (Ren et al., 2023). Protein phosphatase 1 regulatory inhibitor subunit 1 A (PPP1R1A),

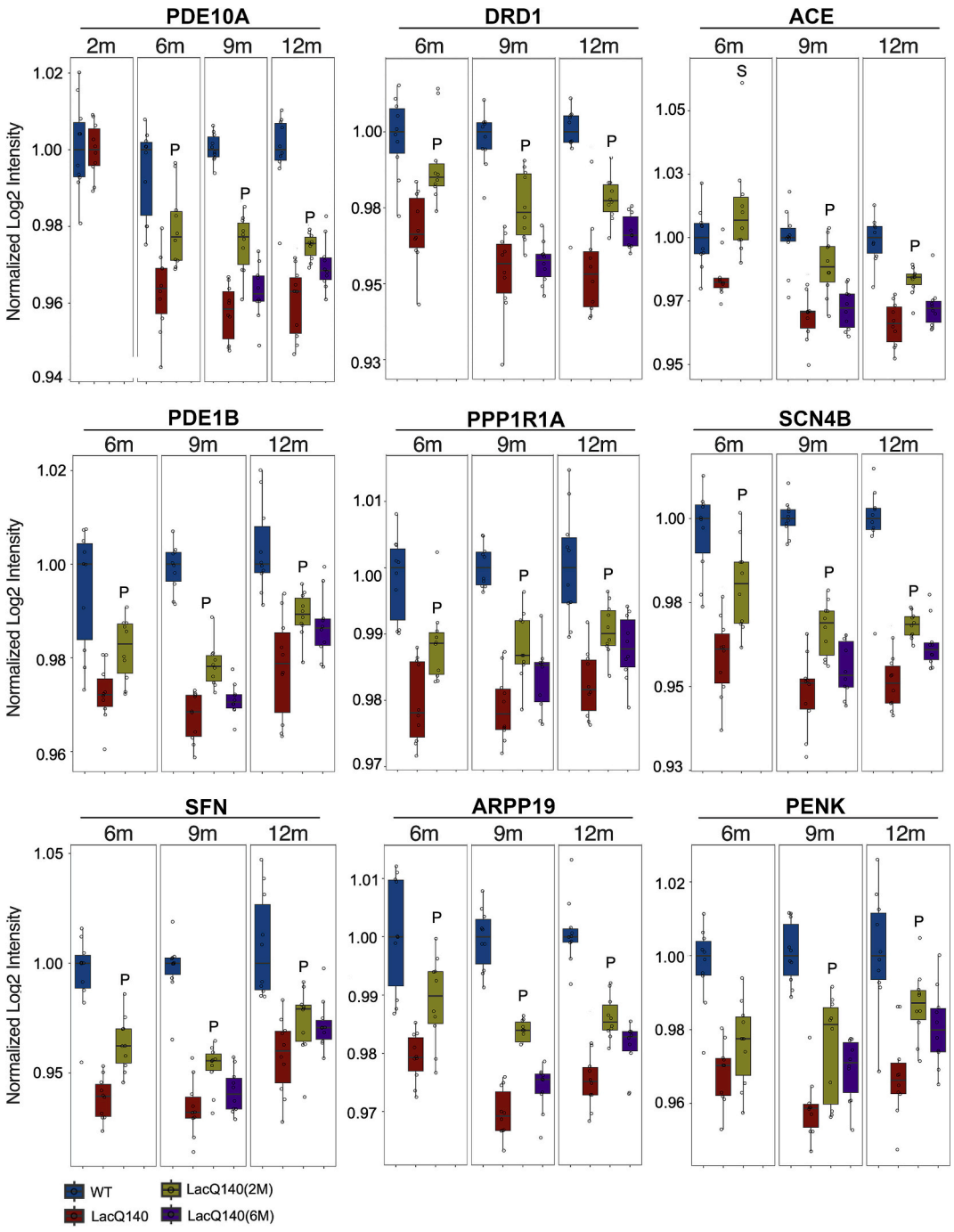

Fig. 5. Proteomic expression of selected proteins. Expression levels are plotted as ratio to WT control at each individual timepoint. Dysregulation of each protein in the striatum of the LacQ140 and reversal of dysregulation is presented. For each m*Htt*-lowering group, the reversal probability assignment is provided (super [S], partial [P]). $N = 9$–10/group (mixed males, females). Data are shown as mean ± SEM.

protein phosphatase 1 regulatory inhibitor subunit 1B (PPP1R1B), stratifin (SFN), sodium channel β-subunit 4 (SCN4B) and proenkephalin (PENK) are detectable in CSF (Barschke et al., 2022; Caron et al., 2022; Hsu et al., 2019) and these proteins will be explored as candidate wet biomarkers in future studies.

PDE10A is highly expressed in medium spiny neurons (MSNs) and regulates cAMP signaling (Nishi et al., 2008; Seeger et al., 2003). It has been reported to be decreased very early in PwHD, and prior to onset of clinical symptoms (Fazio et al., 2020; Mätlik et al., 2024; Niccolini et al., 2015), as well as in mouse models of HD (Bertoglio et al., 2018; Hebb et al., 2004), where it is reduced in a CAG-length-dependent manner (Aaronson et al., 2021). PDE10A also plays a role in integration of dopamine signaling in D_1 and D_2 MSNs (Mota et al., 2021). An imbalance in dopamine signaling is thought to occur in HD (Cepeda et al., 2014; Schwab et al., 2015), and both D_1 and D_2 mRNA and protein expression is reduced in a CAG-length-dependent manner (Aaronson et al., 2021). We determined that PDE10A was not yet dysregulated at 2 months of age, as measured by proteomics, which is the early m*Htt* lowering initiation timepoint. The static readouts (proteomics and ARG) revealed partial preservation of PDE10A out to 12 months of age. *In vivo* PET imaging revealed a significant reduction in PDE10A by 3 months of age in the striatum of the LacQ140 mice. Early m*Htt* lowering (initiated at 2 months of age) resulted in partial preservation of PDE10A with longitudinal PET imaging out to 6 months of age. Since HD mouse

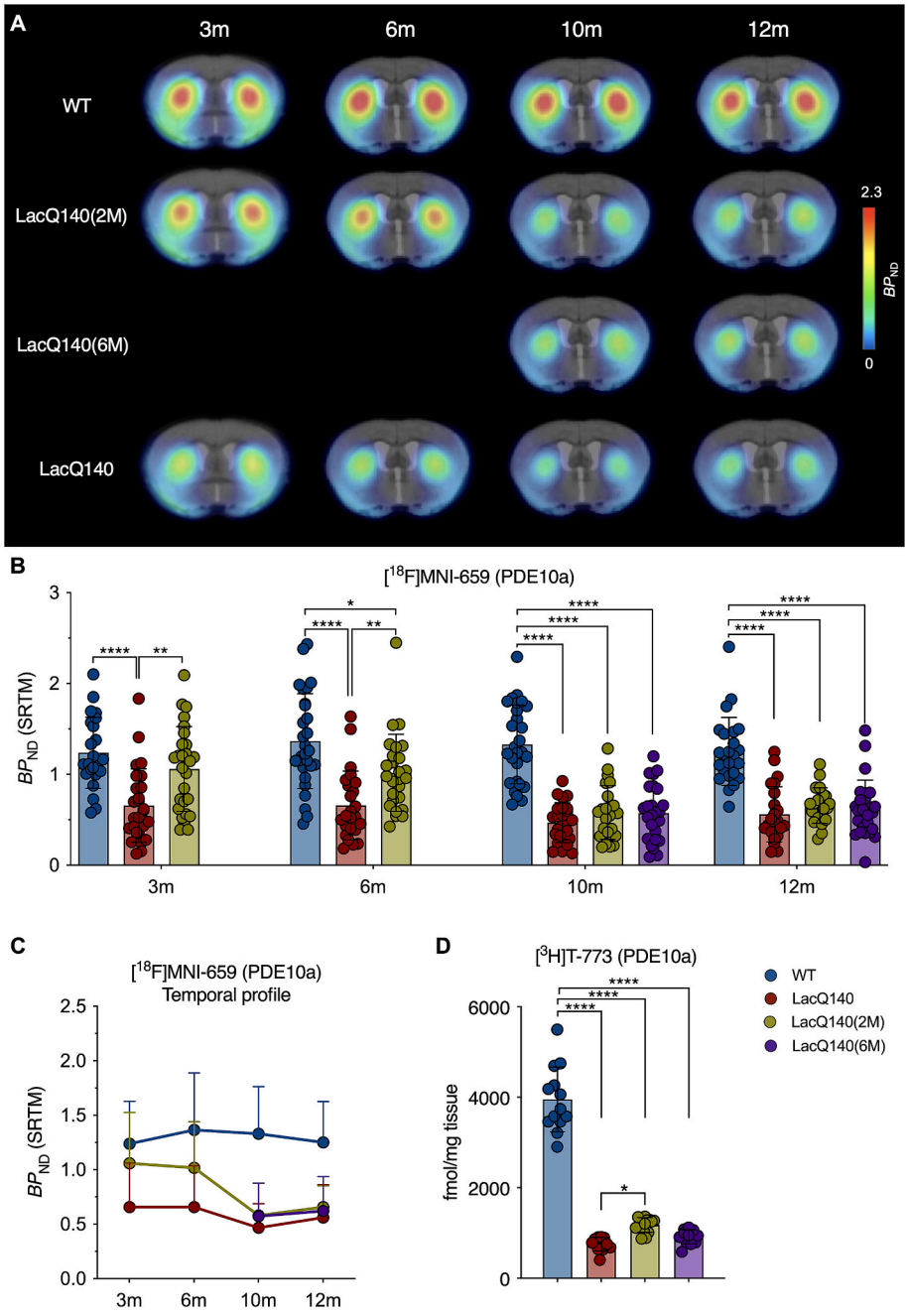

Fig. 6. PDE10A levels were transiently maintained after early m*Htt* lowering. (A) Mean [^{18}F]MNI-659 BP_{ND} parametric maps in the coronal plane of WT, LacQ140, LacQ140(2 M), and LacQ140(6M) at 3, 6, 10, and 12 months of age. (B) Quantification of striatal [^{18}F]MNI-659 BP_{ND}. One-way ANOVA at each time point. 3 m: $F(2,73) = 12.3$, $p < 0.0001$, 6 m: $F(2,75) = 16.1$, $p < 0.0001$, 10 m: $F(3,96) = 38.8$, $p < 0.0001$, and 12 m: $F(3,90) = 26.3$, $p < 0.0001$; $n = 22$–27 mice/ group. (C) Temporal profile of the striatal [^{18}F]MNI-659 BP_{ND}. (D) Specific autoradiographic binding of [^{3}H]T-773 in the striatum at 12 months of age. One-way ANOVA, $F(3,47) = 195.1$, $p < 0.0001$; $n = 12$–14 mice/group. $^{*}p < 0.05$, $^{**}p < 0.01$, $^{****}p < 0.0001$. Data are shown as mean ± SD.

models do not exhibit neuronal loss (Rangel-Barajas and Rebec, 2018), preservation or rescue of PDE10A in a setting with neuronal loss, as observed in PwHD, may be difficult, particularly since the enzyme declines very early in PwHD (Fazio et al., 2020; Niccolini et al., 2015). Nonetheless, the rapid annual decline in PDE10A with PET imaging in PwHD does support its utility as a biomarker for an interventional study that may stabilize PDE10A (Fazio et al., 2020).

Dysregulation of dopamine signaling is prevalent in neurological diseases and there are existing translational PET ligands binding to D_1 and D_2 receptors (Farde et al., 1987). Both D_1 and D_2 receptors undergo significant reduction with disease progression in PwHD (Ginovart et al., 1997; Sedvall et al., 1994) as well as in animal models (Bertoglio et al., 2021; Häggkvist et al., 2017). In the current study, DRD1 was reduced by 6 months of age, but, following m*Htt* lowering, was preserved out to 12 months of age. This is consistent with our unbiased biological pathway enrichment analysis of dysregulated proteins that revealed a high percentage of preserved proteins in the dopamine receptor signaling pathway across all ages examined. In contrast, the loss of D_2R was not even partially preserved in the LacQ140 mice with early or late m*Htt* lowering. Future studies could examine whether *in vivo* microPET imaging for D_1R or $D_{2/3}$R could detect transient beneficial effects of the mHtt lowering at earlier stages. However, it is also possible that a greater degree of m*Htt* lowering is required to preserve $D_{2/3}$R long-term, as was demonstrated with a zinc finger protein repressor strategy that

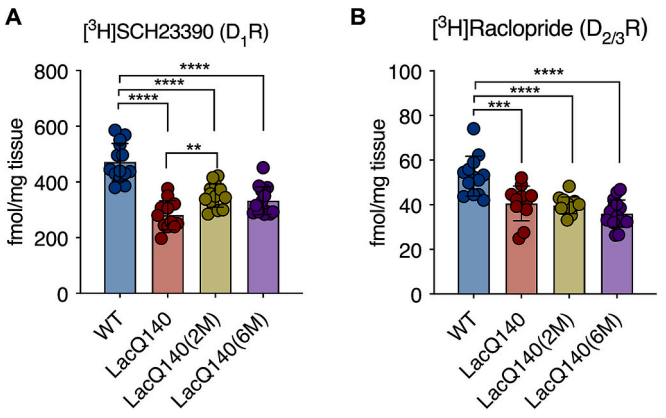

Fig. 7. Evaluation of the dopamine system in the striatum of the LacQ140. (A) Autoradiographic binding of [^{3}H]SCH23390 at 12 months of age. One-way ANOVA, $F(3,51) = 30.1$, $p < 0.0001$. (B) autoradiographic binding of [^{3}H] Raclopride at 12 months of age. One-way ANOVA, $F(3,50) = 15.6$, $p < 0.0001$. n = 12–15 mice/group. $^{**}p < 0.01$, $^{***}p < 0.001$, $^{****}p < 0.0001$. Data are shown as mean ± SD.

targets the expanded CAG repeat to reduce mHTT levels more robustly (Zeitler et al., 2019).

Collectively, this study demonstrates the benefits of early m*Htt* lowering intervention in the LacQ140 mouse model of HD. It is possible that late m*Htt* lowering does not provide significant relief from phenotypes due to cells already passing a critical CAG size threshold due to somatic instability (Aldous et al., 2024; Handsaker et al., 2025; Scahill, 2025; Wang, 2025). Some of the most dysregulated proteomic pathways involved dopamine signaling and synaptic function, and they were readily preserved long-term with early m*Htt* lowering. mHTT, particularly IBs found outside of the nucleus, were very responsive to lowering. Considering that a reduction in PDE10A and D_1R have been demonstrated by imaging in PwHD (Fazio et al., 2020; Ginovart et al., 1997; Niccolini et al., 2015; Sedvall et al., 1994), and this study shows that they are responsive to m*Htt* lowering in the LacQ140 model, PDE10A and D_1R hold potential to serve as imaging biomarkers that are responsive to mHTT lowering. Additionally, we propose SCN4B and ACE as additional wet biomarker candidates. In summary, the ability to measure temporal effects of therapeutic agents on several responsive imaging biomarkers represents a critical tool to understand the biological benefits of *HTT* lowering agents in development of approaching clinical trials.

CRediT authorship contribution statement

Deanna M. Marchionini: Writing – review & editing, Writing – original draft, Visualization, Project administration, Methodology, Formal analysis, Data curation, Conceptualization. **Stef De Lombaerde:** Investigation, Formal analysis. **Joëlle van Rijswijk:** Investigation, Formal analysis. **Franziska Zajicek:** Investigation, Formal analysis. **Liesbeth Everix:** Investigation, Formal analysis. **Alan Miranda:** Investigation, Formal analysis. **Mari J. Aaltonen:** Investigation, Formal analysis. **Carleen M. Kluger:** Investigation, Formal analysis. **Thomas Wild:** Investigation, Formal analysis. **Aglaia Kakoulidou:** Investigation, Formal analysis. **Jannis Gundelach:** Investigation, Formal analysis. **Tim Fieblinger:** Investigation, Formal analysis. **Joachim Fentz:** Investigation, Formal analysis. **Jim Rosinski:** Validation, Formal analysis, Data curation. **John Obenauer:** Formal analysis, Data curation. **Jonathan R. Greene:** Formal analysis, Data curation. **Longbin Liu:** Project administration, Formal analysis. **Ignacio Munoz-Sanjuan:** Formal analysis, Conceptualization. **Marleen Verhoye:** Methodology, Investigation, Formal analysis. **Jeroen Verhaeghe:** Formal analysis, Conceptualization. **Jonathan Bard:** Project administration, Methodology, Formal analysis. **Steven Staelens:** Methodology, Formal analysis, Conceptualization. **Daniele Bertoglio:** Methodology, Investigation, Formal analysis, Conceptualization.

Submission declaration

The work described has not been published previously except in the form of an abstract at a scientific conference.

Funding

This work was supported by the nonprofit CHDI Foundation, Inc.

Declaration of competing interest

CHDI Foundation is a nonprofit biomedical research organization exclusively dedicated to collaboratively developing therapeutics that substantially improve the lives of those affected by Huntington's disease. CHDI Foundation conducts research in a number of different ways; for the purposes of this manuscript, all research was conceptualized, planned and directed by all authors and the University of Antwerp or at the contract research organizations Psychogenics, Evotec SE and Rancho Biosciences. No other potential conflicts of interest exist.

Acknowledgements

We would like to thank Christina Torturo, Kim Cirillo and Sylvie Ramboz at Psychogenics for generation, housing and tissue collection of mice. We would like to thank Rebecca Jörg, Isabella Straub, Barbara Kracher and Christoph Schaab for their support in proteomics sample preparation and analysis. For the *in vivo* imaging studies, the authors thank Philippe Joye, Caroline Berghmans, Eleni Van der Hallen, and Annemie Van Eetveldt of the Molecular Imaging Center Antwerp (MICA) as well as Johan Van Audekerke and Ignace Van Spilbeeck (Bio-Imaging Lab) for their valuable assistance. We also thank Dr. Elisabeth Jonckers (Bio-Imaging Lab) for project coordination.

Glossary/List of abbreviations

ACE	angiotensin converting enzyme
ARG	autoradiography
BP_{ND}	non-displaceable binding potential
CSF	cerebrospinal fluid
CT	computed tomography
DIA	data-independent acquisition
DMSO	dimethyl sulfoxide
DRD1	dopamine receptor D1
FDR	false discovery rate
FOV	field of view
GSORA	gene sets over-representation analysis
HAP40/F8A1	Huntingtin associated protein 40
HD	Huntington's disease
HET	heterozygous
IB	inclusion body
IDIF	image-derived input function
IHC	immunohistochemistry
IPTG	isopropyl β-D-1-thiogalactopyranoside
i.v.	intravenous
LC-MS/MS	liquid-chromatography tandem mass-spectrometry
mHTT	mutant huntingtin protein
m*Htt*	mutant huntingtin mRNA
MRI	magnetic resonance imaging
MSN	medium spiny neuron
NfL	neurofilament light chain
OSEM	ordered subset expectation maximization
PCA	principal component analysis
PDE10A	Phosphodiesterase 10a
PDE1B	Phosphodiesterase 1b
PENK	proenkephalin
PET	positron emission tomography

(*continued on next page*)

(*continued*)

PPP1R1A	protein phosphatase 1 regulatory inhibitor subunit 1 A
PPP1R1B	protein phosphatase 1 regulatory inhibitor subunit 1B
PwHD	people with HD
SCN4B	sodium channel β-subunit 4
s.d.	standard deviation
SEM	standard error of the mean
SFN	stratifin
SRTM	simplified reference tissue modeling
TACs	time-activity curve
VOI	voxels of interest
WT	wildtype

Appendix A. Supplementary data

Supplementary data to this article can be found online at https://doi.org/10.1016/j.nbd.2025.106906.

Data availability

The mass spectrometry proteomics data have been deposited to the ProteomeXchange Consortium via the PRIDE55 partner repository with the dataset identifier PXD054495.

References

Aaronson, J., et al., 2021. HDinHD: a rich data portal for Huntington's disease research. J. Huntingt. Dis. 10, 405–412.

Aldous, S.G., et al., 2024. A CAG repeat threshold for therapeutics targeting somatic instability in Huntington's disease. Brain 147, 1784–1798.

Antonini, A., Leenders, K.L., Eidelberg, D., 1998. [11C]raclopride-PET studies of the Huntington's disease rate of progression: relevance of the trinucleotide repeat length. Ann. Neurol. 43, 253–255.

Ashburner, M., et al., 2000. Gene ontology: tool for the unification of biology. The gene ontology consortium. Nat. Genet. 25, 25–29.

Barschke, P., et al., 2022. Cerebrospinal fluid levels of proenkephalin and prodynorphin are differentially altered in Huntington's and Parkinson's disease. J. Neurol. 269, 5136–5143.

Beaumont, V., et al., 2016. Phosphodiesterase 10A inhibition improves Cortico-basal ganglia function in Huntington's disease models. Neuron 92, 1220–1237.

Bertoglio, D., et al., 2018. MR-based spatial normalization improves [18F]MNI-659 PET regional quantification and detectability of disease effect in the Q175 mouse model of Huntington's disease. PLoS One 13, e0206613.

Bertoglio, D., et al., 2021. Kinetic modelling and test-retest reproducibility for the dopamine D(1)R Radioligand [(11)C]SCH23390 in healthy and diseased mice. Mol. Imaging Biol. 23, 208–219.

Bertoglio, D., et al., 2022a. Development of a ligand for in vivo imaging of mutant huntingtin in Huntington's disease. Sci. Transl. Med. 14, eabm3682.

Bertoglio, D., et al., 2022b. Validation, kinetic modeling, and test-retest reproducibility of [(18)F]SynVesT-1 for PET imaging of synaptic vesicle glycoprotein 2A in mice. J. Cereb. Blood Flow Metab. 42, 1867–1878.

Caron, N.S., et al., 2022. Cerebrospinal fluid biomarkers for assessing Huntington disease onset and severity. Brain Commun. 4, fcac309.

Cepeda, C., et al., 2014. The role of dopamine in Huntington's disease. Prog. Brain Res. 211, 235–254.

Cronin, C.A., Gluba, W., Scrable, H., 2001. The lac operator-repressor system is functional in the mouse. Genes Dev. 15, 1506–1517.

Demichev, V., et al., 2020. DIA-NN: neural networks and interference correction enable deep proteome coverage in high throughput. Nat. Methods 17, 41–44.

DiFiglia, M., et al., 1997. Aggregation of huntingtin in neuronal intranuclear inclusions and dystrophic neurites in brain. Science 277, 1990–1993.

Farag, M., Tabrizi, S.J., Wild, E.J., 2024. Huntington's disease clinical trials update: September 2024. J. Huntingt. Dis. 13, 409–418.

Farde, L., et al., 1987. PET analysis of human dopamine receptor subtypes using 11C-SCH 23390 and 11C-raclopride. Psychopharmacology 92, 278–284.

Fazio, P., et al., 2020. PET molecular imaging of phosphodiesterase 10A: an early biomarker of Huntington's disease progression. Mov. Disord. 35, 606–615.

Gao, L., et al., 2024. Pharmacokinetics and pharmacodynamics of PTC518, an oral huntingtin lowering splicing modifier: a first-in-human study. Br. J. Clin. Pharmacol. 90, 3242–3251.

Ginovart, N., et al., 1997. PET study of the pre- and post-synaptic dopaminergic markers for the neurodegenerative process in Huntington's disease. Brain 120 (Pt 3), 503–514.

Gunn, R.N., et al., 1997. Parametric imaging of ligand-receptor binding in PET using a simplified reference region model. Neuroimage 6, 279–287.

Gutekunst, C.A., et al., 1999. Nuclear and neuropil aggregates in Huntington's disease: relationship to neuropathology. J. Neurosci. 19, 2522–2534.

Häggkvist, J., et al., 2017. Longitudinal small-animal PET imaging of the zQ175 mouse model of Huntington disease shows in vivo changes of molecular targets in the striatum and cerebral cortex. J. Nucl. Med. 58, 617–622.

Handsaker, R.E., et al., 2025. Long somatic DNA-repeat expansion drives neurodegeneration in Huntington's disease. Cell 188, 623–639.e19.

Hebb, A.L., Robertson, H.A., Denovan-Wright, E.M., 2004. Striatal phosphodiesterase mRNA and protein levels are reduced in Huntington's disease transgenic mice prior to the onset of motor symptoms. Neuroscience 123, 967–981.

Herrmann, F., et al., 2021. Pharmacological characterization of mutant huntingtin aggregate-directed PET imaging tracer candidates. Sci. Rep. 11, 17977.

Hickman, R.A., et al., 2022. The distribution and density of huntingtin inclusions across the Huntington disease neocortex: regional correlations with huntingtin repeat expansion independent of pathologic grade. Acta Neuropathol. Commun. 10, 55.

Hsu, W.H., et al., 2019. Combined proteomic and metabolomic analyses of cerebrospinal fluid from mice with ischemic stroke reveals the effects of a Buyang Huanwu decoction in neurodegenerative disease. PLoS One 14, e0209184.

Johnson, G.A., et al., 2010. Waxholm space: an image-based reference for coordinating mouse brain research. Neuroimage 53, 365–372.

Ko, J., et al., 2018. Identification of distinct conformations associated with monomers and fibril assemblies of mutant huntingtin. Hum. Mol. Genet. 27, 2330–2343.

Landles, C., et al., 2020. Subcellular localization and formation of huntingtin aggregates correlates with symptom onset and progression in a Huntington'S disease model. Brain Commun. 2, fcaa066.

Liu, L., et al., 2020. Imaging mutant huntingtin aggregates: development of a potential PET ligand. J. Med. Chem. 63, 8608–8633.

Logan, J., et al., 1990. Graphical analysis of reversible radioligand binding from time-activity measurements applied to [N-11C-methyl]-(−)-cocaine PET studies in human subjects. J. Cereb. Blood Flow Metab. 10, 740–747.

Maat-Schieman, M.L., et al., 1999. Distribution of inclusions in neuronal nuclei and dystrophic neurites in Huntington disease brain. J. Neuropathol. Exp. Neurol. 58, 129–137.

Marchionini, D.M., et al., 2022. Benefits of global mutant huntingtin lowering diminish over time in a Huntington's disease mouse model. JCI. Insight 7.

Mätlik, K., et al., 2024. Cell-type-specific CAG repeat expansions and toxicity of mutant huntingtin in human striatum and cerebellum. Nat. Genet. 56, 383–394.

McColgan, P., et al., 2023. Tominersen in adults with manifest Huntington's disease. N. Engl. J. Med. 389, 2203–2205.

Menalled, L.B., et al., 2003. Time course of early motor and neuropathological anomalies in a knock-in mouse model of Huntington's disease with 140 CAG repeats. J. Comp. Neurol. 465, 11–26.

Miranda, A., et al., 2020. Validation of a spatially variant resolution model for small animal brain PET studies. Biomed. Phys. Eng. Express. 6, 045001.

Mota, É., et al., 2021. Pivotal role of phosphodiesterase 10A in the integration of dopamine signals in mice striatal D(1) and D(2) medium-sized spiny neurones. Br. J. Pharmacol. 178, 4873–4890.

Nesvizhskii, A.I., Aebersold, R., 2005. Interpretation of shotgun proteomic data: the protein inference problem. Mol. Cell. Proteomics 4, 1419–1440.

Niccolini, F., et al., 2015. Altered PDE10A expression detectable early before symptomatic onset in Huntington's disease. Brain 138, 3016–3029.

Nishi, A., et al., 2008. Distinct roles of PDE4 and PDE10A in the regulation of cAMP/PKA signaling in the striatum. J. Neurosci. 28, 10460–10471.

Patrinostro, X., et al., 2018. Essential nucleotide- and protein-dependent functions of Actb/β-actin. Proc. Natl. Acad. Sci. USA 115, 7973–7978.

Rangel-Barajas, C., Rebec, G.V., 2018. Overview of Huntington's disease models: neuropathological, molecular, and behavioral differences. Curr. Protoc. Neurosci. 83, e47.

Reiner, A., Deng, Y.P., 2018. Disrupted striatal neuron inputs and outputs in Huntington's disease. CNS Neurosci. Ther. 24, 250–280.

Ren, F., et al., 2023. (68)Ga-cyc-DX600 PET/CT in ACE2-targeted tumor imaging. Eur. J. Nucl. Med. Mol. Imaging 50, 2056–2067.

Russell, D.S., et al., 2016. Change in PDE10 across early Huntington disease assessed by [18F]MNI-659 and PET imaging. Neurology 86, 748–754.

Sathasivam, K., et al., 2013. Aberrant splicing of HTT generates the pathogenic exon 1 protein in Huntington disease. Proc. Natl. Acad. Sci. USA 110, 2366–2370.

Scahill, R.I., et al., 2025. Somatic CAG repeat expansion in blood associates with biomarkers of neurodegeneration in Huntington's disease decades before clinical motor diagnosis. Nat. Med. 31, 807–818.

Schwab, L.C., et al., 2015. Dopamine and Huntington's disease. Expert. Rev. Neurother. 15, 445–458.

Sedvall, G., et al., 1994. Dopamine D1 receptor number–a sensitive PET marker for early brain degeneration in Huntington's disease. Eur. Arch. Psychiatry Clin. Neurosci. 243, 249–255.

Seeger, T.F., et al., 2003. Immunohistochemical localization of PDE10A in the rat brain. Brain Res. 985, 113–126.

de Sousa Abreu, R., et al., 2009. Global signatures of protein and mRNA expression levels. Mol. BioSyst. 5, 1512–1526.

Spronck, E.A., et al., 2019. AAV5-miHTT gene therapy demonstrates sustained huntingtin lowering and functional improvement in Huntington disease mouse models. Mol. Ther. Methods Clin. Dev. 13, 334–343.

Spronck, E.A., et al., 2021. Intrastriatal administration of AAV5-miHTT in non-human Primates and rats is well tolerated and results in miHTT transgene expression in key areas of Huntington disease pathology. Brain Sci. 11.

Tabrizi, S.J., Ghosh, R., Leavitt, B.R., 2019. Huntingtin lowering strategies for disease modification in Huntington's disease. Neuron 101, 801–819.

Tabrizi, S.J., et al., 2020. Huntington disease: new insights into molecular pathogenesis and therapeutic opportunities. Nat. Rev. Neurol. 16, 529–546.

Turjanski, N., et al., 1995. Striatal D1 and D2 receptor binding in patients with Huntington's disease and other choreas. A PET study. Brain 118 (Pt 3), 689–696.
Wang, N., et al., 2025. Distinct mismatch-repair complex genes set neuronal CAG-repeat expansion rate to drive selective pathogenesis in HD mice. Cell 188, 1524–1544.
Weeks, R.A., et al., 1996. Striatal D1 and D2 dopamine receptor loss in asymptomatic mutation carriers of Huntington's disease. Ann. Neurol. 40, 49–54.
Wu, Y.J., Carson, R.E., 2002. Noise reduction in the simplified reference tissue model for neuroreceptor functional imaging. J. Cereb. Blood Flow Metab. 22, 1440–1452.
Yu, G., et al., 2012. clusterProfiler: an R package for comparing biological themes among gene clusters. Omics 16, 284–287.
Zeitler, B., et al., 2019. Allele-selective transcriptional repression of mutant HTT for the treatment of Huntington's disease. Nat. Med. 25, 1131–1142.